Supporting Information

Multifunctional Self-Healing Superhydrophobic Coating with Rapid Sunlight-Induced Recovery and Photothermal Anti-Icing Capability

Alix Marcelle Sansi Seukep[1,3], Damas Rossel Pandzou[4], Xuan Zhou[1,3], Syeda Andleeb Zahra Naqvi[1,3], Dhandapani Kuzhandaivel[1,3], Abilash Rosario Arockiyasamy[1,3], MD Salman Farsee[1,3], Zixiang Weng[1], Xiaohong Ding[1,2*], Lixin Wu[1*]

[1]Fujian Key Laboratory of Nanomaterials, Fujian Institute of Research on the Structure of Matter, Chinese Academy of Sciences, Fuzhou 350002, PR China

[2]Fujian Provincial Key Laboratory of Eco-Industrial Green Technology, College of Ecological and Resources Engineering, Wuyi University, 354300, Wuyishan, PR China

[3]University of Chinese Academy of Sciences, Beijing 100049, PR China

[4]College of Transportation Engineering, Fujian University of Technology, Fuzhou, Fujian 350118, China

*Corresponding authors.

Xiaohong Ding: dingxh@fjirsm.ac.cn; Lixin Wu: lxwu@fjirsm.ac.cn

Experimental section

1.1 *High-pressure water-jet impingement test*

The coating's dynamic impingement resistance was assessed using a high-pressure water-jetting setup (a programmable rain test chamber, HT-IP9K-1000L). The coated glass substrate was positioned vertically (90° tilt), and a continuous water jet (25 kPa) was applied from a distance of 5 cm at a speed of 10 m/s. The surface was exposed to the jet for increasing durations (0–150 s), after which the WCA and SA were recorded to evaluate changes in wetting behavior.

1.2. Chemical and physical self-healing tests

To evaluate the self-healing capacity of the coatings, two types of damage were induced: chemical and mechanical. Chemical degradation was simulated by treating the coatings for 3 min using an O_2-plasma system. Mechanical damage was inflicted by creating a surface scratch with a new razor blade. Following damage, samples were exposed to simulated sunlight from a xenon lamp solar simulator (CEL-HXF300-T3, Beijing Zhongjiao Jinyuan Technology Co., Ltd., China) for 5 min to activate the healing process. The recovery from chemical damage was quantified by measuring the WCA before and after healing to track the loss and subsequent restoration of superhydrophobicity. Microstructural recovery was assessed by examining scratch morphology using optical microscopy and FE-SEM, comparing the damaged and healed states.

1.3. Mechanical and chemical durability tests

The mechanical robustness of the coatings was evaluated through a series of tests designed to simulate harsh environmental stresses, including sand abrasion, high-pressure water impact, and sandpaper wear.

Sand abrasion resistance. Cyclic sand abrasion tests were conducted by releasing 500 g of silica sand (300–400 μm particle size) from a height of 40 cm onto the coated surface, inclined at 45°. The sand was delivered in 10 increments of 50 g each. Water contact angles (WCAs) and sliding angles (SAs) were measured after each full cycle to quantify the retention of superhydrophobicity.

Water impact resistance. Coatings were subjected to a high-impact water jet spray totaling 5000 L over 24 hours, directed at a 45° angle from 50 cm. The WCAs and SAs were recorded at 4-hour intervals to monitor degradation under sustained hydraulic pressure.

Sandpaper abrasion Test. Samples were placed face-down on 800- or 1000-grit SiC sandpaper and subjected to linear abrasion under a 200 g load. Each 15 cm forward movement constituted one cycle. WCAs and SAs were measured after every 10 cycles, up to a total of 50 cycles. To evaluate the self-healing capability post-abrasion, mechanically stressed coatings were irradiated under simulated sunlight (1.0 sun) for 5 min. Recovery of surface morphology was observed using optical microscopy, and the corresponding restoration of superhydrophobicity was confirmed through WCA and SA measurements.

Tape-peeling adhesion test. Adhesion durability was evaluated using a standard tape-peeling procedure following ASTM D3359. A 3M #600 adhesive tape (25.4 mm width, 50 μm thickness) was firmly applied to the coating under a uniform pressure of 2.6 kPa and then peeled off in a single motion. This process was repeated for multiple cycles, after which the WCA and SA were recorded to assess any changes in surface wettability.

UV Aging resistance evaluation. The coatings were placed in a UV-aging chamber equipped with a 400 W full-spectrum solar simulator, where they were subjected to alternating cycles consisting of 4 h UVA irradiation at 1000 W/m² and 60 °C, followed by 4 h condensation at 50 °C. After designated numbers of cycles, the WCAs and SAs were measured to evaluate the retention of hydrophobic performance.

Chemical stability was evaluated by immersing coatings in varying pH levels: acidic (pH 1), neutral (pH 6), and alkaline (pH 13) solutions for 24 hours. WCA was measured after immersion to assess superhydrophobicity retention. To evaluate self-healing, chemically treated coatings were irradiated under simulated sunlight (1 sun) for 5 min. Surface recovery was characterized using atomic force microscopy (AFM) for topographic analysis, while superhydrophobicity restoration was confirmed through WCA measurements.

1.4. Self-cleaning test

The self-cleaning performance of the MESH coating was evaluated by depositing sand contaminants on both coated and uncoated glass surfaces inclined at 10°. Water droplets (4 mL) were introduced to the upper surface, and contaminant removal efficiency was quantified by comparing residual sand particles after droplet roll-off.

1.5. Dual-mode anti-icing performance

Static anti-icing tests were conducted at −20 °C under 80% relative humidity to simulate cold, humid environments. The experiments were performed in a programmable constant-temperature and humidity chamber (HD-ED702-504K70, Haida Instrument Co., Ltd., China; operating range −40 to 80 °C, ±1 °C, -100 to 100 % RH). Prior to testing, samples were equilibrated at −20 °C/80% RH for 1 h to ensure stable environmental conditions.

Static passive anti-icing performance was evaluated by depositing a 40 μL dyed (methyl red) water droplet onto both coated and uncoated glass substrates at −20 °C/80% RH, and recording the freezing time using digital camera.

Active anti-icing was tested by repeating the droplet freezing assay under 1 sun irradiation while recording the delayed freezing process.

Dynamic passive anti-icing test. Cold water droplets (0 °C, ~40 μL) were continuously dispensed onto a 20°-tilted glass or MESH-coated substrate inside a low-temperature chamber maintained at −10 °C and 80% relative humidity. The onset of freezing, and subsequent ice accumulation were monitored and recorded using a digital camera to determine the dynamic icing resistance.

Active de-icing test. A uniform ice layer was first generated on the sample surfaces under −20 °C and 80% RH. The iced substrates, positioned at a 20° tilt, were then exposed to 1.0-sun irradiation while remaining inside the same low-temperature chamber. The melting and detachment of ice were recorded using a digital camera.

Ice adhesion strength was measured using a using a lab-built force transducer, which detached ice from the surface at 0.1 mm/s. The peak force was recorded, and the average of three tests reported as ice adhesion strength.

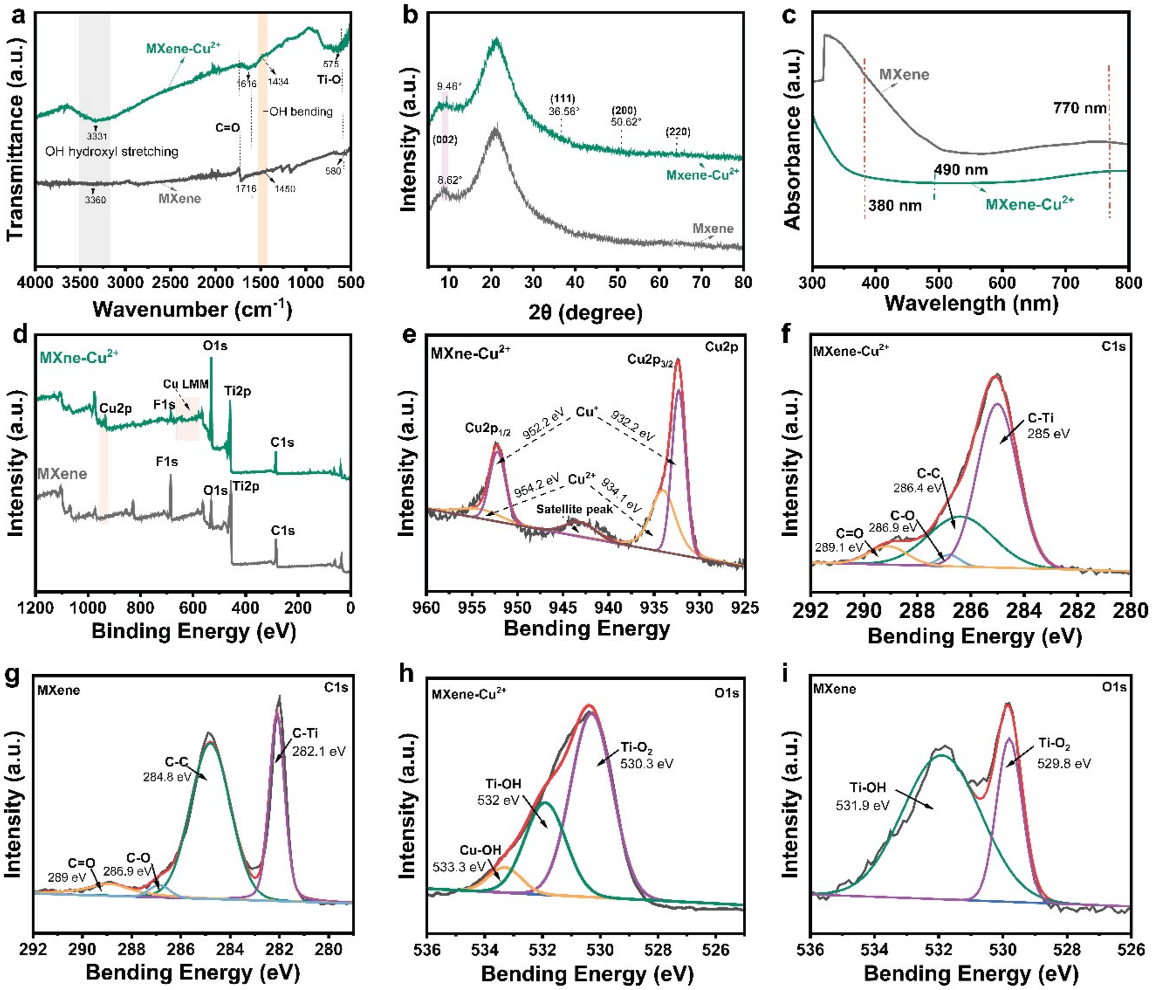

Figure S1. (a) ATR-FTIR spectra, (b) XRD patterns, and (c) UV–vis spectra of MXene and MXene–Cu^{2+}. (d) XPS survey spectra, and (e–i) high-resolution XPS spectra of Cu 2p, C 1s, and O 1s for MXene–Cu^{2+} and MXene, respectively.

The TEM image (Figure S2a) revealed well-defined nanosheet structures decorated with uniformly distributed nanoparticles, while the HRTEM image (Figure S2b) offered a closer view of the lattice fringes, confirming the crystalline nature of the embedded copper species. Notably, the zoomed-in HRTEM image (Figure S2c) displayed distinct lattice planes corresponding to Cu(111), with an interplanar spacing of 0.207 nm, further validating the presence of metallic copper domains. Complementary elemental mapping (Figure S2d) showed homogeneous distribution of Ti, C, O, and Cu across the nanosheet surface, indicating successful doping and intimate integration of Cu^{2+} within the MXene nanosheets. These findings collectively confirm the structural and compositional integrity of the MXene–Cu^{2+} hybrid, supporting its potential for enhanced functional performance.

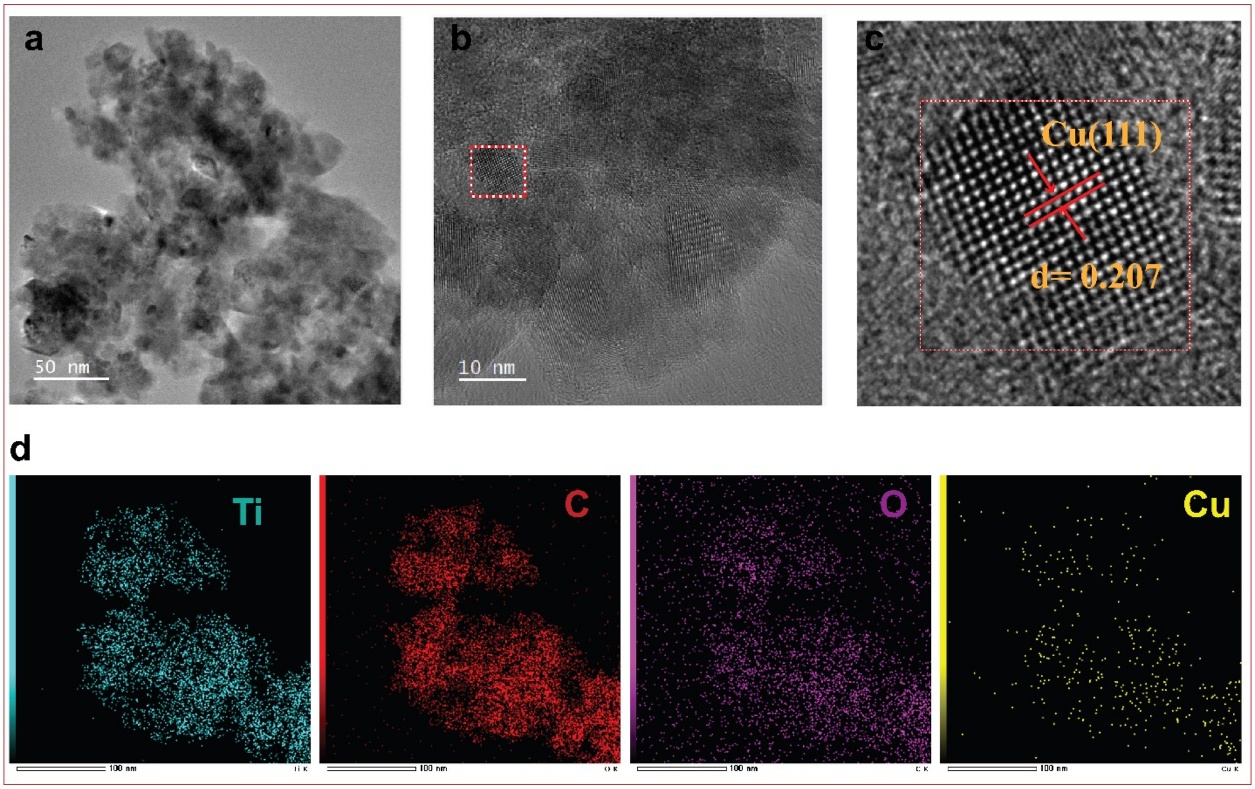

Figure S2. (a–c) TEM and HRTEM images of MXene–Cu^{2+}, and (d) TEM elemental mapping image of MXene–Cu^{2+}.

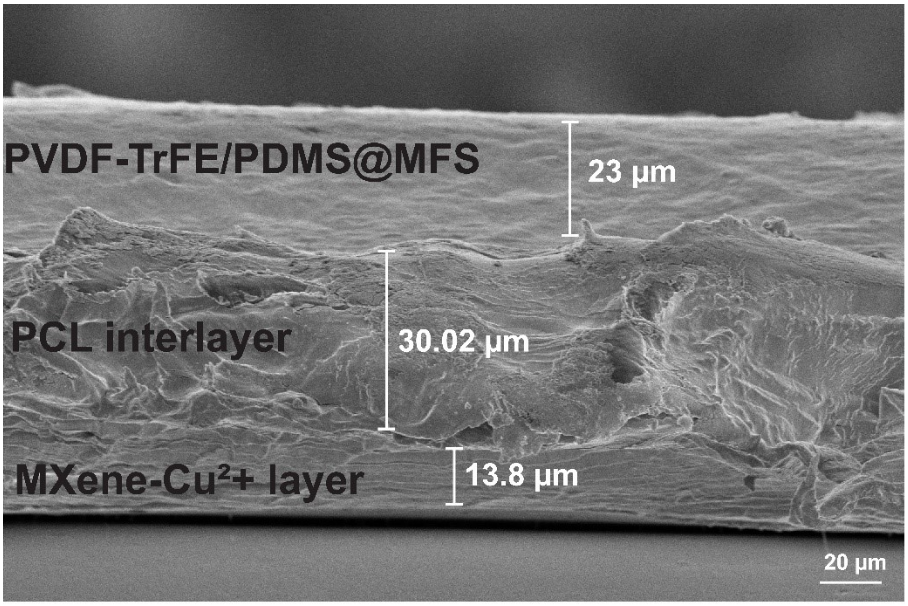

Figure S3. Cross-sectional SEM image of the MESH coating

Impalement Resistance Mechanism

The coating's resistance to liquid impalement under dynamic impact is governed by the pressure balance between the hammer pressure (P_h) of the incoming jet and the capillary pressure (P_c) generated by the surface structure.[1] According to established models' formula S1 and S2:

$$P_h \approx 0.2\rho C v \tag{1}$$

Here, ρ is water density, C is sound velocity, v is impact velocity

$$P_c \approx \frac{2\gamma r \sin^2\left(\frac{\theta_{adv}}{2}\right)}{d^2} \tag{2}$$

Where γ is surface tension, r is particle radius, d is spacing between protrusions, and θ_{adv} is the advancing contact angle.

The equations show that reducing the spacing d between surface features markedly increases P_c, meaning that tightly spaced micro–nano structures are more resistant to impalement.[1]

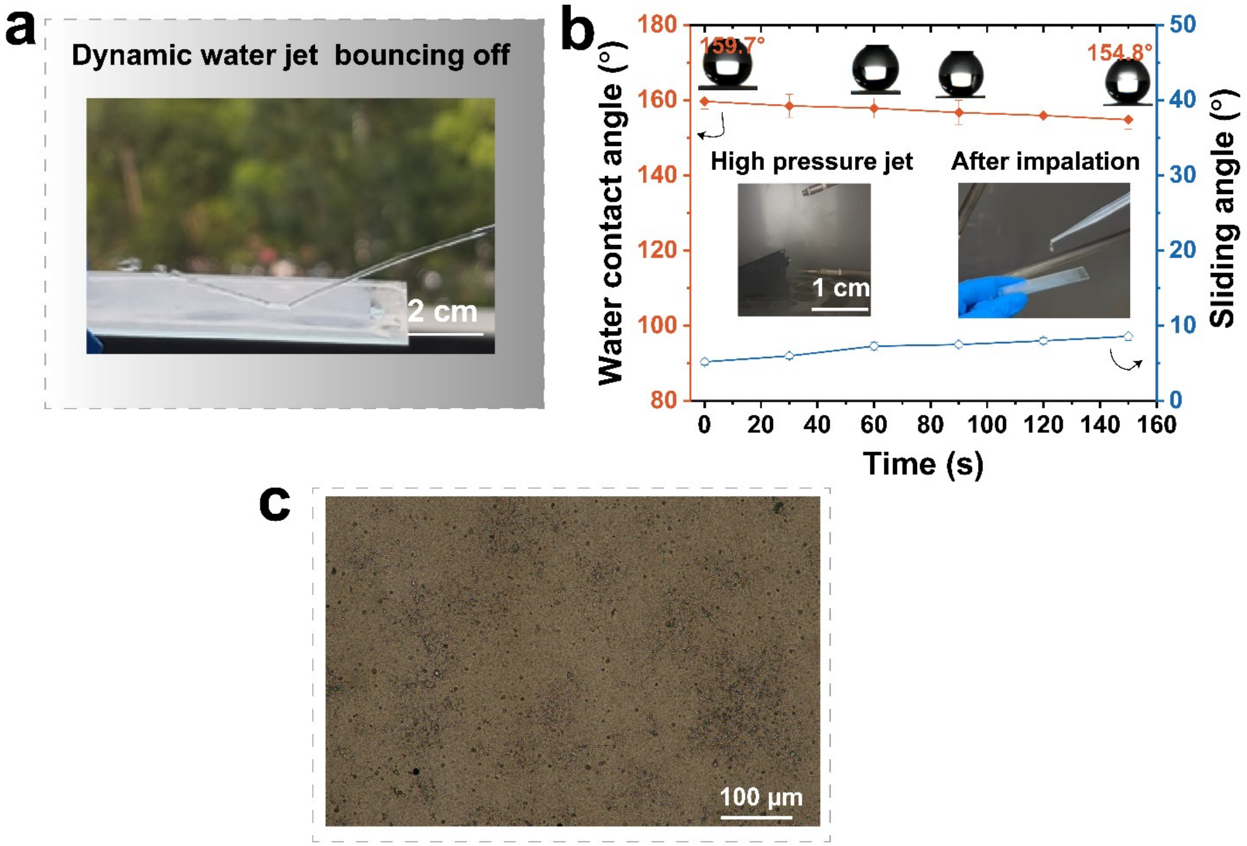

Figure S4. (a) Dynamic water jet bouncing off the MESH coating. (b) Time-dependent evolution of WCA and SA during continuous high-pressure jetting. (c) Microscopic image of the surface after jet impalement

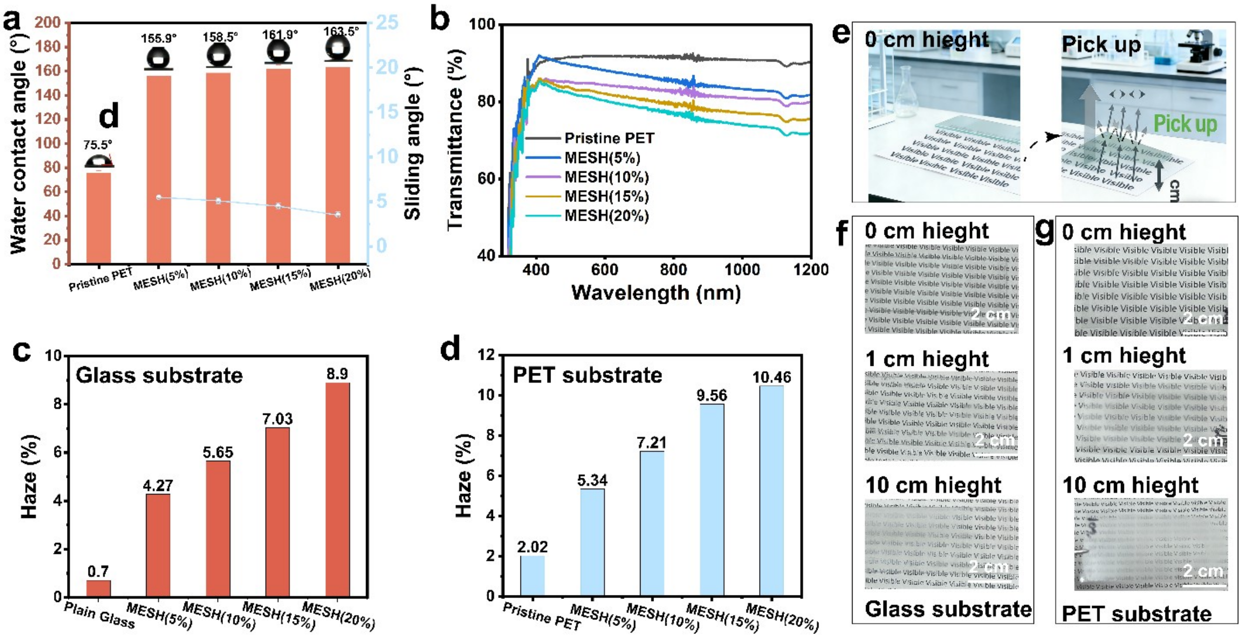

Figure S5. (a) Wettability of MESH coatings on PET substrate at varying filler ratios, showing WCA and SA. (b) Optical transmittance spectra of pristine PET and MESH-coated PET films. (c–d) Haze values at 550 nm for MESH coatings on glass (c) and PET (d) substrates (e) Schematic illustration of the measurement configuration for transmittance and haze using a paper sheet as background. (f–g) Photographs showing text visibility through MESH-coated glass (f) and PET (g) placed directly on the paper sheet (0 cm) and at distances of 1 cm and 10 cm, demonstrating the balance between high transmittance and controlled haze.

Photothermal Conversion Efficiency

To evaluate the photothermal conversion efficiency (η) of the MXene–Cu^{2+} coating under simulated solar illumination, we adopted a modified energy balance approach analogous to the method used by Fan et al.[2] Since the system involves a solid coating on a glass substrate without phase transition, the stored energy is entirely sensible heat. The efficiency was calculated by comparing the thermal energy stored by the sample to the solar energy absorbed during illumination.

(1) *Thermal energy stored by the coated substrate is define by*:

$$Q_{\mathbf{stored}} = m_{eff} \cdot C_{p,eff} \cdot (T_{max} - T_0) \qquad (4)$$

Where Q_{stored} is total sensible heat stored (J), m_{eff} the effective mass (g) and $C_{p,\text{ eff}}$ specific heat capacity of the sample $(J \cdot g^{-1} \cdot K^{-1})$, T_{max} maximum temperature during irradiation $({}^{\circ}C)$, and T_0 initial temperature $({}^{\circ}C)$

The effective mass is given by:

$$m_{eff} = \rho \cdot A \cdot d \qquad (5)$$

2) *Solar energy received and absorbed by the coating define by:*

$$Q_r = P \cdot S \cdot t_{\mathbf{heat}} \qquad (6)$$

Where Q_r is total incident solar energy (J), P the solar intensity $(W \cdot cm^{-2})$, S is illuminated area (cm^2), and t_{heat} irradiation time to reach $T_{max}(s)$

To account for the fraction of light absorbed by the MXene- Cu^{2+} layer, the absorbance at λ (A_λ) was used:

$$Q_{r,abs} = Q_r \cdot \left(1 - 10^{-A_\lambda}\right) \qquad (7)$$

(3) Photothermal conversion efficiency is calculated by:

$$\eta = \frac{Q_{\mathbf{stored}}}{Q_{r,\mathbf{abs}}} = \frac{m_{eff} \cdot C_{p,\mathbf{eff}} \cdot (T_{max} - T_0)}{P \cdot S \cdot t_{\mathbf{heat}} \cdot \left(1 - 10^{-A_\lambda}\right)} \qquad (8)$$

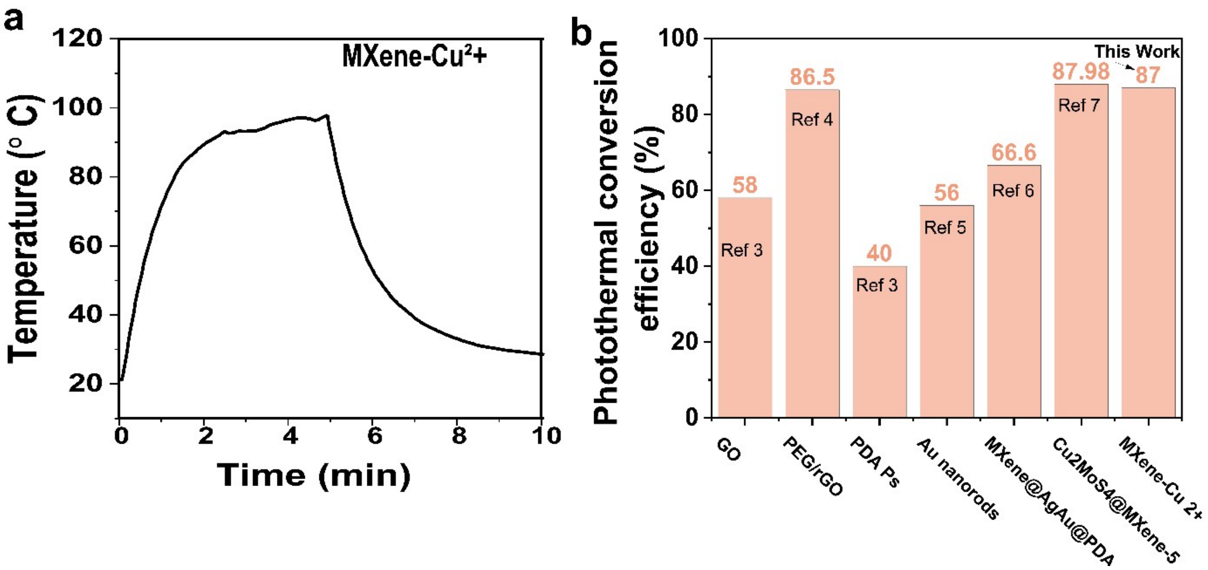

Figure S6. (a) Temperature–time profile of MXene–Cu^{2+} under simulated solar irradiation (1 sun, 5 min heating and 5 min cooling). (b) Comparison of photothermal conversion efficiency (η) for MXene–Cu^{2+} and benchmark materials including GO,[3] PEG/rGO,[4] PDA Ps,[5] Au nanorods,[3] MXene@AgAu@PDA,[6] and Cu$_2$MoS$_4$@MXene.[7]

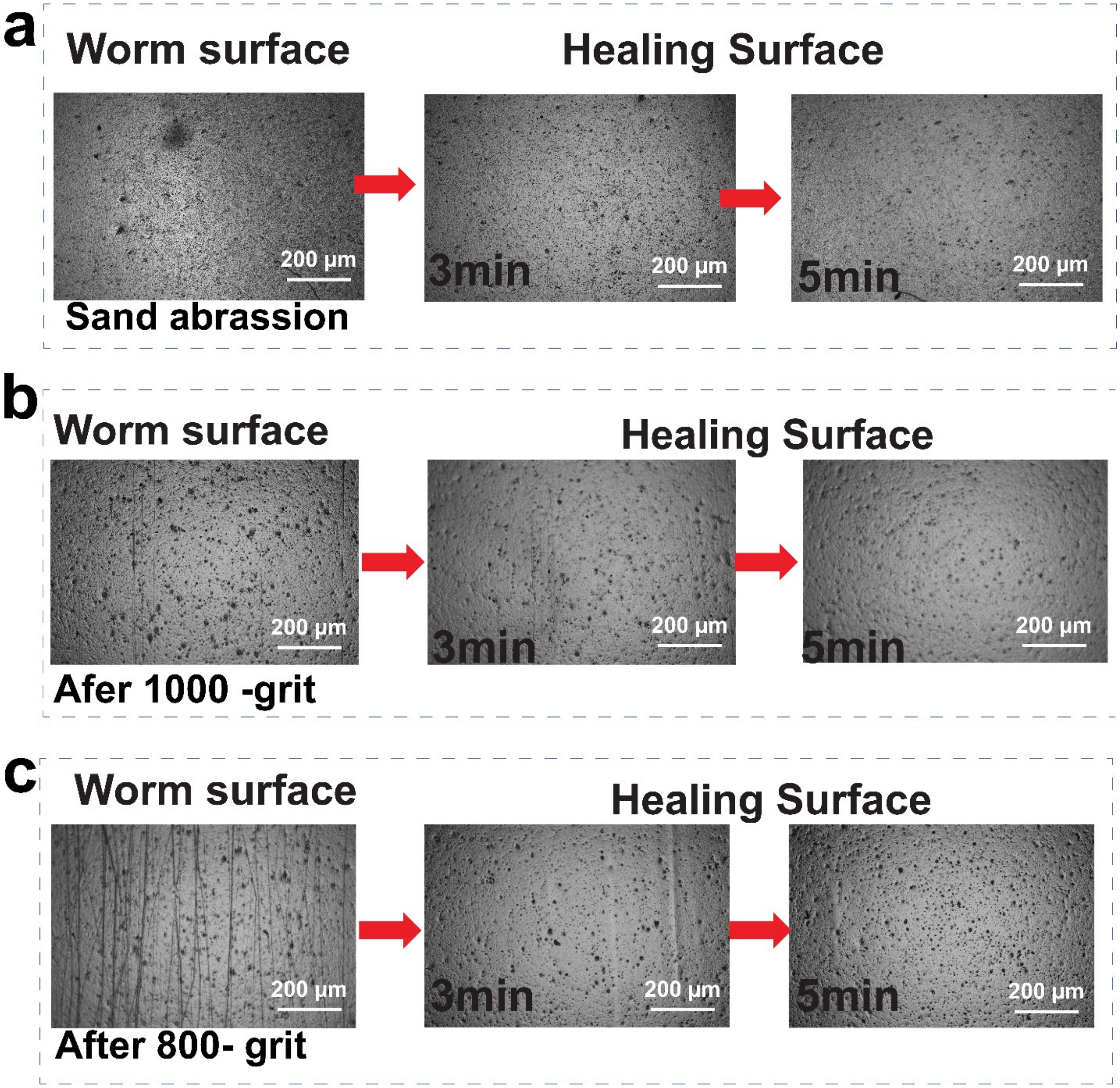

Figure S7. a-c) post-impact healed micrograph images of MESH coating. Sand falling cycle (a), Sandpaper abrasion cycle under 1000 grit (b) and 800 grit(c)

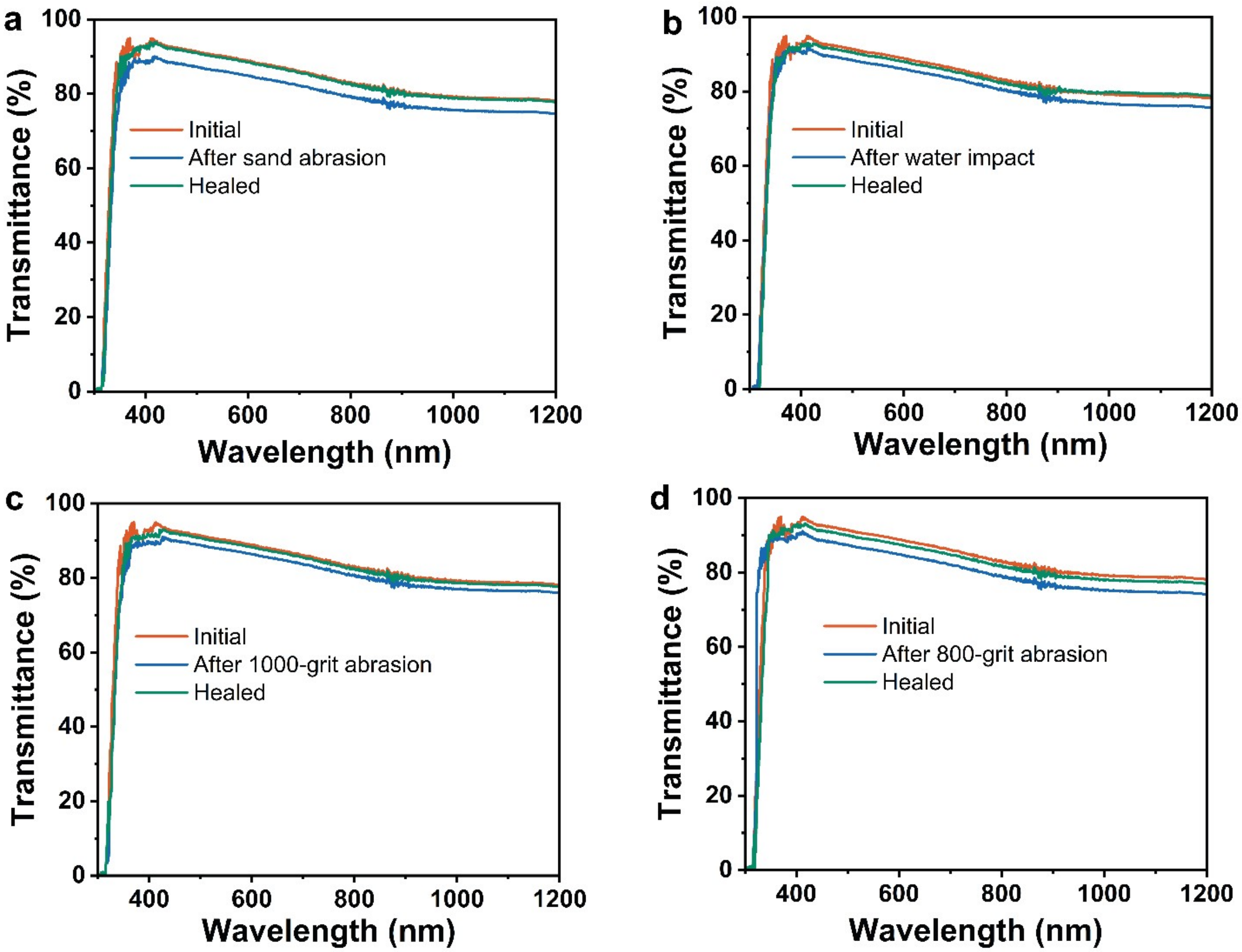

Figure S8. Optical transmittance spectra of the MESH coating at the initial state and after post-mechanical testing and healing, including (a) sand falling test, (b) water impact test, and sandpaper abrasion tests on (c) 1000-grit and (d) 800-grit surfaces, respectively.

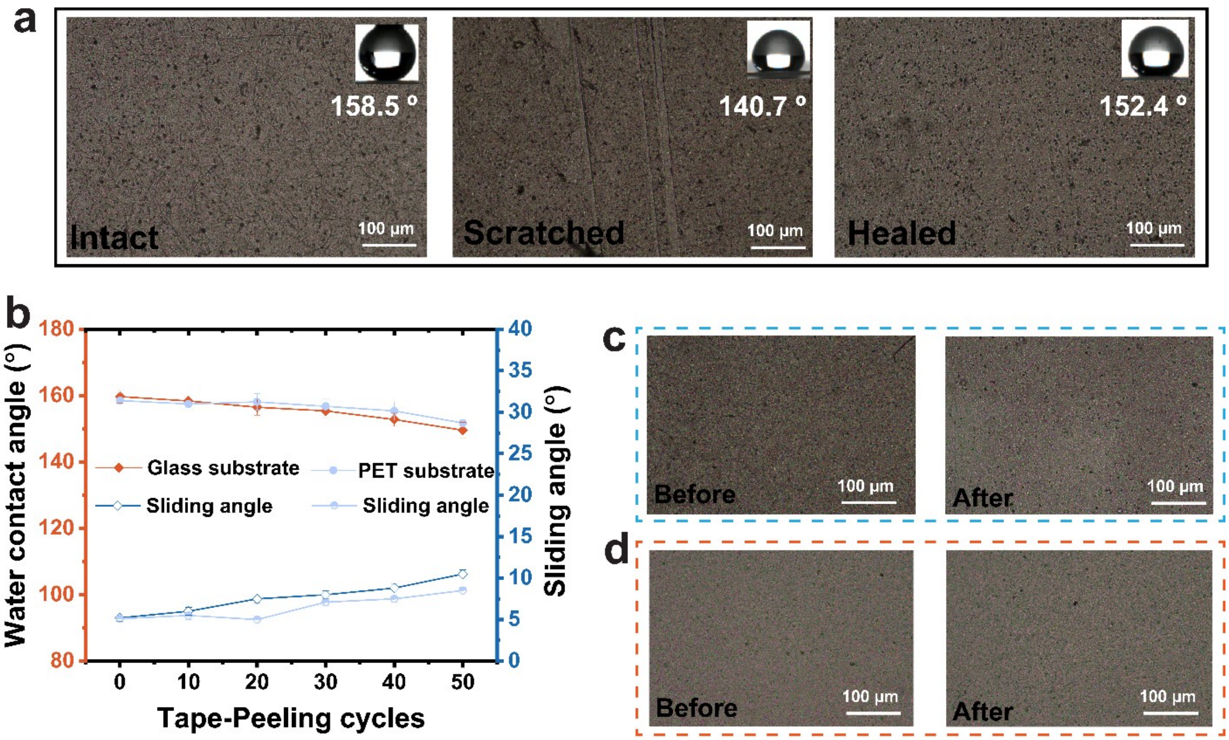

Figure S9. a. Microscopic images of MESH- coated PET substrate at initial, and after scratched and healing process under 1 sun (5 min) (inset is corresponding WCA). b- Relationship between WCA and SA of MESH coating on Glass and PET substrate as a function tape peeling cycles. c- d Microscopic images of MESH coating before and after tape-peeling test on PET and glass substrates, respectively.

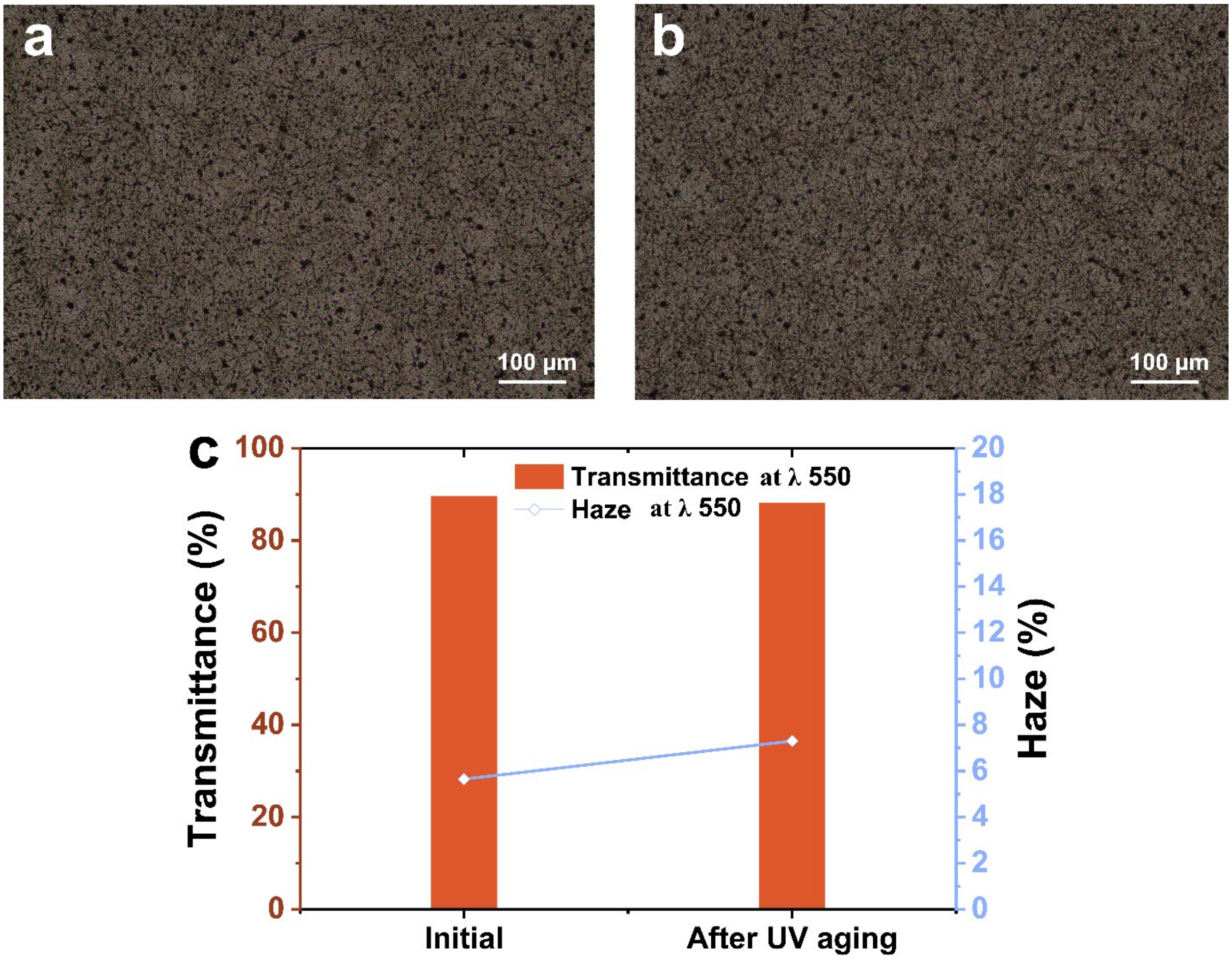

Figure S10. Micrograph images of MESH coating before and after UV aging test. Transmittance and haze value of MESH coating before and after UV aging test.

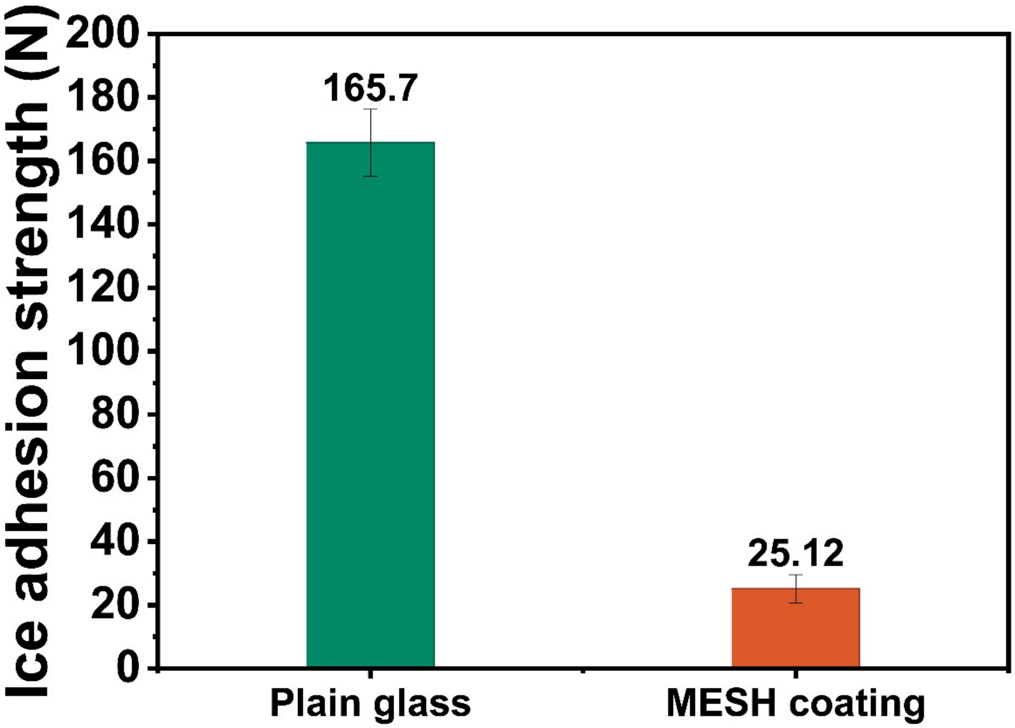

Figure S11. Ice adhesion strength of plain glass and the MESH coating.

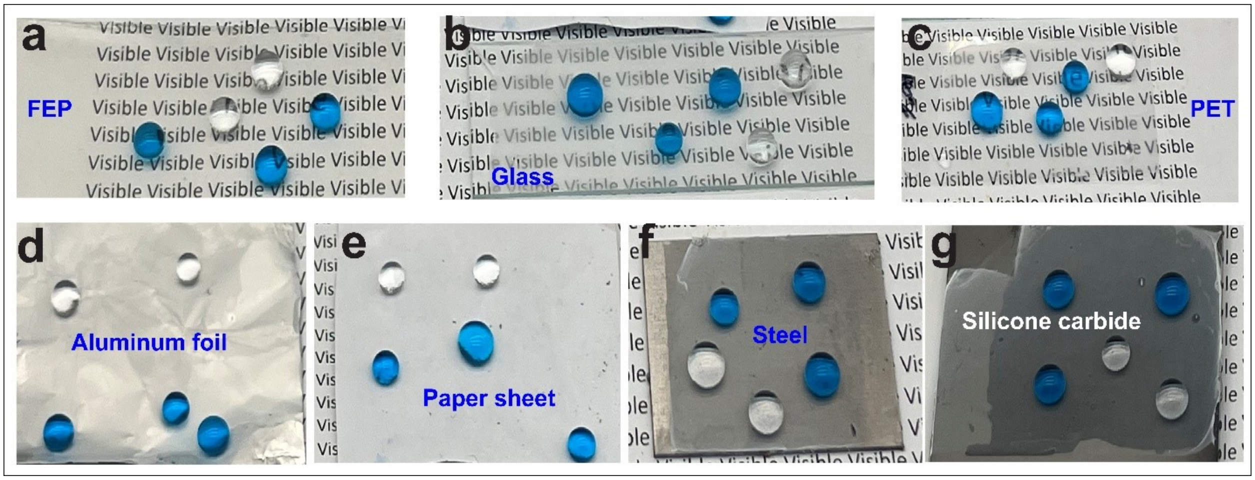

Figure S12. MESH coatings applied to various substrates, including (a) fluorinated ethylene propylene (FEP), (b) glass, (c) polyethylene terephthalate (PET), (d) Aluminum foil, (e) Paper-sheet, (f) Steel, and (g) Silicon carbide, each shown with its corresponding water droplet (dye methyl blue and none-dye water).

Table S1. Comparative summary of superhydrophobic self-healing coatings from this work and recent studies.

Material	Method	Chemical self-healing		Physical self-healing		Functionality		Ref
		Properties	*Scenarios*	*Properties*	*Scenarios*	*Self-cleaning*	*Anti-icing*	
DDA-PDA@CNTs	One-pot	O_2 plasma-repair	150°C, **10 min**	Surface structure repair	89.9°C, **10 min**	Yes	Yes	8
BPDI/SiO_2	Dual cross-linking, spray	plasma etching	Spontaneous room temp	Surface reorganization	UV	Yes	Not stated	9
PU/SiO_2@HD-POS	Spray-coating,	HD-POS migration	room temp			Yes	Yes	10
Al/ZnO-P.I.Z-FAS@PDA	spray	chemical repair	**40 min**, room temp	scratch repair	**5 min**, 80°C (photothermal)	Yes	Yes	11
POEG/ Fluorinated carbon black	Two-step spray			Surface structure repair	Heat treatment	Not stated	Yes	12
DTMS@PDA@ SiO_2@CNTs/epoxy	One-step spray	chemical corrosion	NIR irradiation	scratch repair		Yes	Not stated	13
ZIF-7@ZnG@ PFDS/epoxy	MOF-based, spray	NaCl				Yes	Yes	14
PDA-Cu^{2+}-GO/ODA/PDMS	Layered, chelation, spray	O_2 plasma	1-sun irradiation	Scratch repair	1-sun irradiation	Yes	Not stated	15
PU/ZnO@PDA-SA	disulfide-bonded			Scratch repair	70°C, **1h**	Yes		16
ZnO@MPDA/silicone latex	Blending, stimuli-responsive	controlled release	UV/NIR/ acid/base			Yes	Not stated	17
PEG/Fe_3O_4-SA/polyamide-epoxy	Hydrogen bonding		4 h room temp, **10 min** oven			Yes	Yes	18
CNT@SiO_2/epoxy	Spray	48 h alkali cycles	4 h room temperature, **10 min** 80 °C oven			Not stated	Yes	19
PDMS-IPDI-TFB/PDA NPs	Spray		Sunlight, room temp			Yes	Yes	20
MXene–Cu^{2+}/PCL/PVDF-TrFE/PDMS	Electrospinning assisted coating	O_2 plasma	1-sun, **5 min**	Scratch repair	1-sun, **5 min**	Yes	Yes	This work

References

1. H. Teisala, F. Geyer, J. Haapanen, P. Juuti, J. M. Mäkelä, D. Vollmer and H. J. Butt, *Adv Mater*, 2018, **30**, 1706529.

2. R. Fan, N. Zheng and Z. Sun, *Sol. Energy Mater. Sol. Cells*, 2022, **237**, 111572.

3. O. A. Savchuk, J. Carvajal, J. Massons, M. Aguiló and F. Díaz, *Carbon*, 2016, **103**, 134-141.

4. W. Luo, M. Zou, L. Luo, Y. Ma, W. Chen, X. Hu, Q. Li and X. Jiang, *J. Energy Storage*, 2024, **78**, 109950.

5. Y. Li and D. Wang, *Chin. J. Pharm*, 2021, **19**, 81-86.

6. G. Liu, H. Wang, C. Xu, Q. Fang, H. Wang, Y. Xu, M. Sang, S. Xuan and L. Hao, *J. Mater. Chem. B*, 2023, **11**, 10678-10691.

7. L. Li, J. Zhang, Y. Lin, Y. Zhang, S. Li, Y. Liu, Y. Zhang, L. Shi, S. Yuan and L. Guo, *Front. Bioeng. Biotechnol.*, 2022, **10**, 902312.

8. Y. Li, H. Li, J. Wu, X. Yang, X. Jia, J. Yang, D. Shao, L. Feng, S. Wang and H. S. Song, *Appl. Surf. Sci*, 2022, **600**, 154177.

9. J. Tao, L. Dong, Y. Wu, X. Liu, J. Xie, H. Wu and Q. Ran, *Compos. Pt. B-Eng*, 2024, **273**, 111245.

10. Y. Li, B. Li, X. Zhao, N. Tian, J. Zhang, *ACS Appl. Mater. Interfaces*, 2018, **10**, 39391-39399.

11. T. Zhang, J. Deng and L.-Z. Zhang, *Prog. Org. Coat*, 2023, **180**, 107569.

12. K. Li, J. Xiang, J. Zhou, X. Su, H. Xie, S. Lin, Z. Xiao, W. Huang, C. Zhao and H. Chen, *Prog. Org. Coat*, 2023, **177**, 107415.

13. J. Liu, W. Huang, G. Cui, X. Xing and J. Liu, *Process Saf. Environ. Prot.*, 2025, **195**, 106759.

14. G. Zhu, J. Su, C. Yin, H. Li, Y. Yao, L. Zhang, X. Yao, X. Zhang and F.-Q. Liu, *Appl. Surf. Sci.*, 2023, **622**, 156907.

15. C. Lee, S. Ji, S. Oh, S. Park, Y. Jung, J. Lee and H. Lim, *Nanoscale Adv.*, 2022, **4**, 761-771.

16. C. Li, P. Wang, D. Zhang and S. Wang, *ACS Appl. Mater. Interfaces*, 2022, **14**, 45988-46000.

17. X. Ni, C. Li, Y. Lei, Y. Shao, Y. Zhu and B. You, *ACS Appl. Mater. Interfaces*, 2021, **13**, 57864-57879.

18. X. Wang, L. Tang, S. Fan and W. Fan, *Nanomaterials*, 2024, **14**, 1981.

19. Z. He, H. Xu, Y. Zhou and Y. Tan, *J Mater Res Technol*, 2024, **30**, 2609-2619.

20. Y. Wu, L. Dong, X. Shu, Y. Zhang and Q. Ran, *ACS Appl. Mater. Interfaces*, 2025, **17**, 18852-18868.